

# Prospects of detecting gamma-ray emission from galaxy clusters: cosmic rays and dark matter annihilations

Anders Pinzke<sup>1,\*</sup>, Christoph Pfrommer<sup>2,†</sup> and Lars Bergström<sup>3,‡</sup>

<sup>1</sup>*University of California - Santa Barbara, Department of Physics, CA 93106-9530, USA*

<sup>2</sup>*Heidelberg Institute for Theoretical Studies (HITS),*

*Schloss-Wolfsbrunnengasse 33, DE - 69118 Heidelberg, Germany and*

<sup>3</sup>*The Oskar Klein Centre for Cosmoparticle Physics, Department of Physics, Stockholm University, AlbaNova University Center, SE - 106 91 Stockholm, Sweden*

(Dated: March 24, 2011)

... to be written...

PACS numbers: 95.35.+d, 95.85.Pw, 98.62.Gq, 98.65.-r, 98.70.Sa

## I. INTRODUCTION

Dark matter has been searched for in direct detection experiments [1], at accelerators [2–4] and also in indirect detection experiments looking for signals in the cosmic-ray spectra of antiprotons, positrons, neutrinos and all of the electromagnetic spectrum from radio waves to gamma rays [5]. So far, the improvements in direct detection sensitivity have put this method into focus, but the situation may change considerably the coming few years as the CERN LHC experiments collect data, and new gamma-ray detectors are being planned, such as the CTA [6]. In fact, it has recently been pointed out [7] that a dedicated ground-based gamma-ray detector would have potential that goes far beyond that of the other methods, depending on presently unknown parameters in the particle physics models for dark matter.

Among the astrophysical systems which will be very interesting to detect, and study, with coming gamma-ray detectors (Fermi, HESS, MAGIC, VERITAS, and eventually large detectors like CTA) belong galaxy clusters. The most promising directions in which to search for a gamma-ray annihilation signal (from the annihilation process itself, and also the accompanying bremsstrahlung and inverse Compton components coming from charged particles produce in the annihilations) are basically three:

1. The galactic centre (g.c.). This is where all numerical simulations of cold dark matter predict the highest density. However, the detailed dark matter density in the very central part is difficult to predict, due to a possibly very complicated interplay between baryons, dark matter, and the central galactic black hole. Also, it is a very crowded region with many gamma-ray sources like pulsars and other supernova remnants, which have to be subtracted from the data to extract the dark matter induced signal. In fact, there is a recent claim of an indication of a relatively light dark matter particle contribution to the gamma-ray flux from the g.c. [8], but other hypotheses seem to work at least as well [9].

2. The dwarf spheroidal galaxies orbiting the Milky Way, like Segue-1, Ursa Minor, Draco, Sagittarius, Sculptor, Carina or Willman-1 [10–12]. The problem here is that the nature of many of these small, dark matter-dominated galaxies is not entirely clear, and the velocity dispersion estimates are based on rather small numbers of stars. Tidal disruption and confusion with star clusters are other complications. Thus the dark matter density profile is very uncertain for most of them. Nonetheless, by stacking the data together from many dwarf spheroidals these uncertainties can be made less severe, and preliminary results from Fermi-LAT shows this method to give quite promising results [13].

3. Galaxy clusters. This possibility has been less studied, however we noted in a previous Letter [14] that there are certain advantages that work in favour of this possible target for gamma-ray detection of dark matter annihilation. Galaxy clusters constitute the most massive objects in our Universe that are forming today. This causes their DM subhalo mass function to be less affected by tidal stripping compared to galaxy sized halos that formed long ago. The annihilation luminosities of the DM halo component for e.g. the Virgo cluster and the Draco dwarf scales in a way (see [14]) that the ratio of gamma-ray luminosities from the smooth components is around 4, in favour of Virgo. In addition, there may be a further enhancement due to substructure, which to a large extent should be unaffected by tidal disruption, at least in the outer regions. According to a recent estimate [15], more massive haloes tend to have a larger mass fraction in subhalos. For example, cluster size haloes typically have 7.5 per cent of the mass within  $r_{200}$  in substructures of fractional mass larger than  $10^{-5}$ , which is 25 per cent higher than galactic haloes [16].

For a satellite dwarf galaxy, however, once it is accreted by the Milky Way, the outer regions are severely affected by tidal stripping. The longer a satellite has been part of our Galaxy, and the closer it comes to the center during its pericentral passage, the more material is removed [17].

In this paper, we will investigate in some more detail the potential of several of the most promising galaxy clusters to yield an annihilation gamma-ray yield which could be observable with present and planned gamma-ray detectors.

---

\* apinzke@physics.ucsb.edu

† pfrommer@cita.utoronto.ca

‡ lbe@fysik.su.se

For previous work related to dark matter in clusters, see, e.g., [18, 19].

**Anders, insert your flux table for various clusters, and discuss it**

This yields Fornax ( $M_{200} = 10^{14} M_{\odot}$ ) and Virgo ( $M_{200} = 2.1 \times 10^{14} M_{\odot}$ ) as the prime targets for DM observations, Perseus ( $M_{200} = 7.7 \times 10^{14} M_{\odot}$ ) for CR induced emission and we additionally decide in favor of the well studied cluster Coma ( $M_{200} = 1.4 \times 10^{15} M_{\odot}$ ) for comparison.

## II. THEORY

### A. Astrophysics

The differential photon flux within a given solid angle  $\Delta\Omega$  along a line-of-sight (los) is given by

$$\frac{dF_{\gamma}}{dE_{\gamma}} \equiv \frac{d^3 N_{\gamma}}{dA dt dE_{\gamma}} = \frac{1}{2} \int_{\Delta\Omega} d\psi \sin \psi \frac{dS_{\gamma}}{dE_{\gamma}}(\psi, E_{\gamma}), \quad (1)$$

where

$$\frac{dS_{\gamma}}{dE_{\gamma}}(\psi, E_{\gamma}) = \int_{\Delta\Omega} d\Omega \int_{\text{los}} dl q_{\text{sum}}(E_{\gamma}, r) \Lambda(\theta), \quad (2)$$

and  $S_{\gamma}(\psi, > E_{\gamma})$  denotes the surface brightness above the photon energy  $E_{\gamma}$ . The integration along the line-of-sight  $l$ , in the direction  $\psi$  that the detector is pointing, is parameterized such that the radius of the source  $r = \sqrt{l^2 + D^2 - 2Dl \cos \Psi}$ , where  $D$  is the distance to the source from the galactic center and  $\cos \Psi \equiv \cos \theta \cos \psi - \cos \varphi \sin \theta \sin \psi$ . The angular integration  $d\Omega = \sin \theta d\theta d\varphi$  is performed over a cone centered around  $\psi$  and the opening angle  $\Delta\Omega$  is typically taken to be a few times the point spread function (PSF)  $\theta_{\text{res}}$ . The limited angular resolution results in a probability that a photon coming from a direction  $\psi'$  is instead reconstructed to a direction  $\psi$ , where the underlying probability distribution follow a Gaussian:

$$\Lambda(\theta) = \frac{1}{2\pi\theta_{\text{res}}^2} \exp\left[-\frac{\theta^2}{2\theta_{\text{res}}^2}\right], \quad \text{where } \theta = \psi' - \psi. \quad (3)$$

We denote the total source function by  $q_{\text{sum}}(E_{\gamma}, r)$ , where we include contributions from four main processes; leptophilic DM annihilating to  $\mu^+/\mu^-$  decaying to  $e^+/e^-$  pairs that up-scatter background photons (IC), leptophilic DM emitting final state radiation (FSR), DM benchmark models where neutralino annihilations generate electrons that up-scatter background photons (BM-IC) and emit a continuum as well as final state radiation (BM-Cont), and CR induced  $\pi^0$ 's decaying into gamma-rays. The source function is given by

$$q_{\text{sum}}(E_{\gamma}, r) = q_{\pi^0-\gamma}(E_{\gamma}, r) + \sum_i q_{\text{sm},i}(E_{\gamma}, r) B_{\text{tot},i}(\sigma_v, r) \quad (4)$$

where  $q_{\pi^0-\gamma}(E_{\gamma}, r)$  denotes the CR to gamma-ray source function (see Sect. II A 2 and [20] for more details). The total differential boost factor for DM is the product of enhancement factors from SFE  $B_{\text{sfe}}(\sigma_v)$  (see Sect. II B 1) and from substructure enhancement over the smooth halo contribution  $B_{\text{sub},i}(r) = 1 + q_{\text{sub}}(r)/q_{\text{sm},i}(r)$  (see Sect. II A 1) and is denoted by  $B_{\text{tot},i}(r, \sigma_v) = B_{\text{sfe}}(\sigma_v) B_{\text{sub},i}(r)$ . The DM source function from the smooth halo for each process is written on the form:

$$q_{\text{sm},i}(E_{\gamma}, r) = \sum_j \frac{dN_{\gamma,j}}{dE_{\gamma}} \Gamma_j(r). \quad (5)$$

We represent the annihilation rate density with  $\Gamma_j = (\rho/m_{\chi})^2 \langle \sigma v \rangle_j / 2$ , where  $j$  runs over all  $\gamma$ -ray producing channels each with the spectrum  $\frac{dN_{\gamma,j}}{dE_{\gamma}}$  and annihilation cross-section  $\langle \sigma v \rangle_j$ . The DM density is modeled by an Einasto density profile

$$\rho_{\text{ein}}(r) = \rho_{-2} \exp\left\{-\frac{2}{\alpha} \left[\left(\frac{r}{r_{-2}}\right)^{\alpha} - 1\right]\right\}, \quad \alpha = 0.17, \quad (6)$$

that is slightly shallower than the conventional Navarro-Frenk-White (NFW) profile in the center, but provide a better fit to simulated DM halos [21]. We denote the density where the profile has a slope of  $-2$  by  $\rho_{-2}$ , and the radius by  $r_{-2}$ . Assuming that all the flux from an NFW profile originate from within the scale radius  $r_s = r_{200}/c$ , and all the flux from an Einasto profile originate within  $r_{-2} = r_{200}/c$ , it follows that  $\rho_{-2} = \rho_s/4$ . The virial radius  $r_{200}$  of a halo is defined to be the radius at which the mean density within is a factor  $\Delta = 200$  times the critical density  $\rho_c$  of the universe. The characteristic density of the NFW profile  $\rho_s = (\Delta \rho_c / 3) c^3 / (\log(1+c) - (c/(1+c)))$ , where the halo mass dependent concentration parameter  $c$  is derived from a power-law fit to cosmological simulations with  $M_{200} \gtrsim 10^{10} M_{\odot}$  [22],

$$c = 3.56 \times \left(\frac{M_{200}}{10^{15} M_{\odot}}\right)^{-0.098}. \quad (7)$$

This mass scaling agrees well with [23] for cluster-mass halos after converting the concentration definitions according to [24].

#### 1. Substructures

High-resolution DM simulations of the Milky Way (MW) find vast amount of substructures in the periphery of DM halos. Since the rate of which DM is annihilating depends on the density squared, the resulting flux is boosted compared to the smooth density distribution. Recent simulations suggest a boost from substructures of the order of ten up to a few 100 [25, 26] for a MW size halo. Based on the result from [27], we find the best fit [28] to the luminosity from smooth substructures (i.e.

substructures within substructures are not included) inside radius  $r$  with

$$L_{\text{sub}}(< r) = 0.76 C_1 C_2(M_{200}) L_{200\text{sm}} x^{0.95x^{-0.27}}, \quad (8)$$

where  $L_{200\text{sm}}$  is the luminosity from the smooth halo without substructures within  $r_{200}$  and  $x = \left(\frac{r}{r_{200}}\right)$ . The first normalization constant is given by

$$C_1 = \left(\frac{M_{\text{res,sim}}}{M_{\text{lim}}}\right)^{0.226}, \quad (9)$$

where  $M_{\text{res,sim}} = 10^5 M_\odot$  is the minimum subhalo mass in the MW simulation, and  $M_{\text{lim}}$  the free streaming mass. Here we assume that the power-law scaling relation in Eq. (9) is valid down to the minimum mass of DM halos, which is conventionally in the cold dark matter universe [29, 30] taken to be  $10^{-6} M_\odot$ . Note that potentially the power-law could flatten towards smaller mass scales although current simulations show no hits of such a behaviour and in addition we are approaching the asymptotic behavior in the power spectrum on these scales (CHECK). For DM halos more (less) massive than the MW we expect a larger (smaller) boost from substructures, simply because of the larger (smaller) mass range down to the minimum mass  $M_{\text{lim}}$ . We capture this halo mass dependence with the second normalization in Eq. (8):

$$C_2(M_{200}) = \left(\frac{M_{200}}{M_{200\text{sim}}}\right)^{0.226}, \quad (10)$$

where  $M_{200,\text{sim}} = 1.9 \times 10^{12} M_\odot$  is the mass of the MW halo in the simulation [27].

In Fig. 1 we compare the radial dependence of the accumulative luminosity from different smooth cluster density profiles shown by solid lines. to the substructure boosted luminosity from the

## 2. Cosmic-ray induced gamma-ray emission

The formation process of a galaxy cluster is a very energetic processes that induces both turbulence as well as frequently occurring merging and accretion shocks. These processes are thought to accelerate large quantities of relativistic non-thermal electrons and protons to high energies. On smaller scales, such as galaxies, there is convincing evidence of such non-thermal populations. Especially, in the MW, the cosmic rays are observed directly as well as indirectly through radio, X-ray, and gamma-ray emission. On larger scales of the order of few 100 kpc up to Mpc, there are a vast number of observations of radio emission coming from radio mini halos in the center of cooling flow clusters, radio relics in the periphery of clusters [31] as well smooth giant radio halos that have been observed in more than 50 clusters [32, 33]. This emission is expected to emerge from synchrotron emitting cosmic-ray electrons although the precise origin of

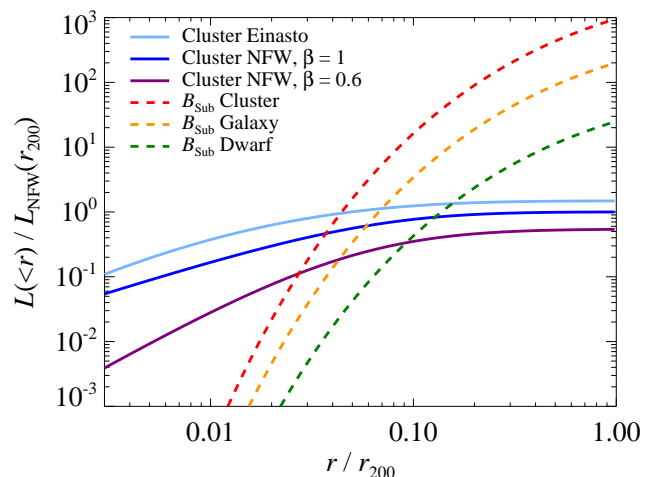


FIG. 1. Radial dependence of various luminosity contributions. The solid lines show the accumulative smooth luminosity from a cluster with the mass  $M_{200} = 10^{15} M_\odot$  for three different density profiles; an Einasto profile with  $\alpha = 0.17$  (light blue), a cuspy NFW profile with  $\beta = 1.0$  (dark blue), and a core NFW profile with  $\beta = 0.6$  (purple). The dashed lines show the accumulative luminosity from substructures for three different mass scales; an  $M_{200} = 10^{15} M_\odot$  galaxy cluster (red), an  $M_{200} = 10^{12} M_\odot$  galaxy (orange), and an  $M_{200} = 10^8 M_\odot$  dwarf galaxy (green). All luminosities have been normalized with the luminosity within  $r_{200}$  from a cuspy NFW profile. Note the large expected boost from substructures in clusters ( $\sim 1000$ ), and the relative small boost in dwarf galaxies ( $\sim 20$ ).

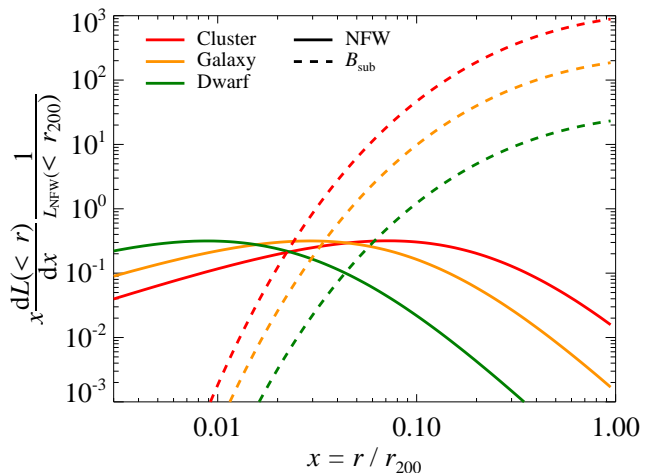


FIG. 2. Volume weighted luminosity for different at different scales. The solid lines show the emissivity from a NFW density profile for three different mass scales; a  $M_{200} = 10^{15} M_\odot$  galaxy cluster (red), a  $M_{200} = 10^{12} M_\odot$  galaxy (orange), a  $M_{200} = 10^8 M_\odot$  dwarf galaxy (green). The dashed lines show the emissivity from substructures for the same three mass scales. All emissivities have been normalized with the luminosity from a NFW profile within  $r_{200}$ .

especially the electrons in giant radio halos is still not settled. If the electrons are of hadronic origin, which seems quite natural due to the long cooling time of cosmic ray protons (CRs) that allows for both an extended and large population of CRs to build up over the cluster history [34].

When the CRs interact with ambient gas protons, it results in the production of both charged and neutral pions that decay into electrons, neutrinos, and gamma-rays. The cluster gamma-ray emission is crucial in this respect as it potentially provides the unique and unambiguous evidence of CR populations in clusters through observing the  $\pi^0$  bump at about 100 MeV in the spectra. We adopt the spectrally and spatially universal gamma-ray model developed by Pinzke & Pfrommer [20] to estimate the emission from decaying  $\pi^0$ :s that dominates over the inverse Compton emission from primary and secondary electrons above 100 MeV in clusters. The gamma-ray formalism was derived from high resolution simulations of clusters of galaxies that included radiative hydrodynamics, star formation, supernova feedback, and followed CR physics using a novel formulation that trace the most important injection and loss processes self-consistently while accounting for the CR pressure in the equation of motion [35–37]. We note that the overall normalization of the CR and gamma-ray distribution scales with the maximum acceleration efficiency at structure formation shock waves. Following recent observations at supernova remnants [38] as well as theoretical studies [39], we adopt a realistic value of this parameter and assume that 50% of the dissipated energy at strong shocks is injected into CRs while this efficiency rapidly decreases for weaker shocks [36].

The gamma-ray source function from decaying  $\pi^0$ :s induced by CRs interacting with ambient gas  $q_{\text{CR}} \propto \rho_{\text{gas}} r h_{\text{OCR}}$

mention that gamma rays induced by protons are especially good targets for cherenkov telescopes since the emission trace the gas density and CR density

## B. Particle physics

### 1. Leptophilic models

Sommerfeld enhancement, electron spectra

### 2. Supersymmetric dark matter

neutralino, benchmark models, continuum emission, electron spectra

### 3. Final state radiation

The photon spectrum from resulting from FSR is universal with only a weak dependence of the underlying

particle physics model. The photon yield from this process is given by (see e.g. [40])

$$\frac{dN_{X\bar{X}}}{dx} \approx \frac{\alpha Q_X^2}{\pi} \mathcal{F}_X(x) \log \left[ \frac{4m_X^2(1-x)}{m_X^2} \right]. \quad (11)$$

Here, the normalized photon energy  $x = E_\gamma/m_X c^2$ ,  $\alpha = e^2/\hbar c$  is the fine-structure constant,  $Q_X^2$  and  $m_X$  the charge and mass of the particle  $X$ , respectively. The function  $\mathcal{F}_X(x)$  depends on the spin of the final state and is given by

$$\mathcal{F}_{\text{fermion}}(x) = \frac{1 + (1-x)^2}{x} \quad (12)$$

for fermions.

## C. Radiative processes

### 1. Inverse Compton

The source function of inverse Compton emission resulting from DM annihilating is given by

$$q_{\text{IC}}(E_\gamma, r) = \int dE_e \frac{dn_e}{dE_e} P_{\text{IC}}(E_\gamma, E_e), \quad (13)$$

where  $P_{\text{IC}}$  is derived by convolving the IC cross-section with the differential target photon number density:

$$P_{\text{IC}} = \frac{3\sigma_{\text{T}} m_e^2 c^5}{4E_e^2} \int \frac{n_{\text{ph}}(E_{\text{ph}}) dE_{\text{ph}}}{E_{\text{ph}}} \times \left[ 2q \ln q + (1+2q)(1-q) + \frac{1}{2} \frac{(\Gamma_e q)^2}{1+\Gamma_e q} (1-q) \right], \quad (14)$$

where

$$\Gamma_e = \frac{4E_{\text{ph}} E_e}{(m_e c^2)^2}, \quad \text{and} \quad q = \frac{E_\gamma}{\Gamma_e (E_e - E_\gamma)}. \quad (15)$$

We account for two major contributions to the radiative background field  $n_{\text{ph}}$ ; the IR and UV light coming from emitting dust and starlight where  $n_{\text{ph}} \equiv \frac{d^2 N_{\text{ph}}^{cl}}{dV dE_{\text{ph}}} (E_{\text{ph}}, r) = \frac{u_{sd}^{cl}(E_{\text{ph}}, r)}{E_{\text{ph}}^2}$  and  $u_{sd}^{cl}(E_{\text{ph}}, r)$  is given by Eq. (30). We model the CMB photon spectrum as a photon gas that is isotropically distributed and follows a black body spectrum with temperature  $T$ :

$$n_{\text{ph}}(E_{\text{ph}}) = \frac{d^2 N_{\text{ph}}}{dV dE_{\text{ph}}} = \frac{1}{\pi^2 (\hbar c)^3} \frac{E_{\text{ph}}^2}{\exp(E_{\text{ph}}/k_B T) - 1}. \quad (16)$$

Here the typical energy of a photon before scattering is given by  $\langle E_{\text{ph}} \rangle = \epsilon_{\text{ph}}/n_{\text{ph}} \approx 2.70 k_B T$ , where  $n_{\text{ph}}$  and  $\epsilon_{\text{ph}}$  are the number- and energy-density derived by integrating  $n_{\text{ph}}(E_{\text{ph}})$  and  $E_{\text{ph}} n_{\text{ph}}(E_{\text{ph}})$  over the photon energy  $E_{\text{ph}}$ , respectively.



The equilibrium spectrum of the electrons plus positrons in Eq. (13) is given by  $\frac{dn_e}{dE_e}$  and derived from the CRe diffusion equation:

$$\frac{\partial}{\partial t} \left( \frac{dn_e}{dE_e} \right) = \nabla \left[ D(E_e, \mathbf{x}) \nabla \frac{dn_e}{dE_e} \right] + \frac{\partial}{\partial E_e} \left[ b(E_e, \mathbf{x}) \frac{dn_e}{dE_e} \right] + Q(E_e, \mathbf{x}), \quad (17)$$

where  $D(E_e, \mathbf{x})$  the diffusion coefficient and  $b(E_e, \mathbf{x})$  the electron energy loss term. The source function  $Q(E_e, \mathbf{x})$  shows the number of particles produced per unit time, energy and volume element that are produced at the position  $\mathbf{x}$ :

$$Q(E_e, r) = \sum_f \frac{dN_e^f}{dE_e}(E_e) B_f \Gamma(r). \quad (18)$$

The subscript  $f$  ... (see cola), and  $B_f$  is the branching factor. Here  $\frac{dN_e^f}{dE_e}$  denote the differential number of electrons plus positrons resulting from an annihilation event. For neutralinos annihilating directly into an electron and positron we model the differential spectrum with  $\frac{dN_e^f}{dE_e} = 2\delta(E_e - m_\chi c^2)$ . We use DarkSUSY to compute both the spectra when neutralinos annihilate directly into a  $\mu^+$  and  $\mu^-$  in the leptophilic model as well as in the four BM models where a fraction of the annihilating neutralinos is converted into electrons and positrons (see [10] and references therein, also see fit).

The electrons and positrons lose their energy on a timescale that is shorter than the diffusive timescale in the ICM of galaxy clusters for CRe energies above MeV (CHECK). Hence, we neglect the first term of the r.h.s. in Eq. 17, and derive an expression for the equilibrium number density:

$$\frac{dn_e}{dE_e}(E_e, r) = \frac{1}{b(E_e, r)} \int_{E_e}^{m_\chi c^2} dE'_e Q(E'_e, r), \quad (19)$$

$$b(E_e, r) = \tilde{b} \left[ \frac{B_{\text{CMB}}^2}{8\pi} + \frac{B^2(r)}{8\pi} + u_{sd}(r) \right] E_e^2, \quad (20)$$

$$\tilde{b} = \frac{4\sigma_{\text{T}} c}{3(m_e c^2)^2}. \quad (21)$$

Here we have included three main loss processes for the electrons;  $B_{\text{CMB}} = 3.24(1+z)^2 \mu\text{G}$  denotes the equivalent field strength of the CMB, we parameterize the magnetic field of the galaxy cluster by  $B(r) = 3\mu\text{G} [n_e(r)/n_e(0)]^{0.7}$ , which follows from flux frozen magnetic fields. In the following subsection we derive a semi-analytic formula that estimates the energy density of the dust and starlight component  $u_{sd}(r)$  given by Eq. (30).

#### IC – dust and starlight

Galaxy clusters are typically characterized by the hot gas in the ICM and the collection of gravitationally bound galaxies. The emission in the IR and UV wavelengths emerge from dust and starlight in both the galaxies and the ICM (e.g. [41] and [42]). Most of this radiation leaks out from the galaxy into the ICM, which explains the very similar spectral shape for these wavelengths. We use the

light from galactic dust and starlight that is emitted in the IR and UV band and is accurately measured for the ISM [41]. We model these spectra through a fit to the galactic spectra presented in [41]. We extract the spatial cluster profile of the emission from a stacked analysis of Sloan Digital Sky Survey (SDSS) data at the redshift  $\sim 0.25$  [43]. Finally, we derive the normalization for the emission from the galaxy cluster using the IR to X-ray luminosity relation presented in the IR cluster luminosity analysis [44].

#### Spectra – galactic

best fit, IR with a power-law function, UV with three power laws, similar to Porter, vary normalization to account for uncertainties, taken at  $r = 0$  in the galaxy

$$\begin{aligned} E_{\text{ph}}^2 \frac{d^2 N_{\text{ph}}^{\text{gal}}}{dE_{\text{ph}} dV} &\equiv u_{sd}^{\text{gal}}(E_{\text{ph}}) \\ &= u_{\text{ir}}^{\text{gal}}(E_{\text{ph}}) + u_{\text{uv}}^{\text{gal}}(E_{\text{ph}}) \end{aligned} \quad (22)$$

$$\begin{aligned} u_{\text{uv}}^{\text{gal}}(E_{\text{ph}}) &= \frac{23 \text{ eV}}{\text{cm}^3} \left( \frac{1.23 \text{ eV}}{E_{\text{ph}}} \right)^{1.9} \\ &\times \left[ 1 + \left( \frac{2.04 \text{ eV}}{E_{\text{ph}}} \right)^{20} \right]^{-\frac{1.9}{20}} \\ &\times \left[ 1 + \left( \frac{0.78 \text{ eV}}{E_{\text{ph}}} \right)^{20} \right]^{-\frac{2.6}{20}} \end{aligned} \quad (23)$$

$$\begin{aligned} u_{\text{ir}}^{\text{gal}}(E_{\text{ph}}) &= \frac{40 \text{ eV}}{\text{cm}^3} \left( \frac{0.0144 \text{ eV}}{E_{\text{ph}}} \right)^{4.9} \\ &\times \left[ 1 + \left( \frac{0.0144 \text{ eV}}{E_{\text{ph}}} \right)^{1.9} \right]^{-4.9}, \end{aligned} \quad (24)$$

#### Spatial distribution - galaxy cluster

Instead of modelling the surface brightness with a de Vaucouleurs with the addition of a power law, we use a double beta profile model for simplicity of deprojection.

$$S(\text{mag arcsec}^{-2}) = \mathcal{M}_\odot + 21.572 - 2.5 \log_{10} S(L_\odot \text{ pc}^{-2}) \quad (25)$$

[45] where the sun's absolute magnitude in the red band is given by  $\mathcal{M}_\odot = 27.1$  [46], and the luminosity of the sun by  $L_\odot = 3.85 \cdot 10^{33} \text{ erg s}^{-1}$ .

surface brightness double  $\beta$  models

$$S_{\text{IR}}(r_\perp) = \sum_{i=1}^2 S_i \left[ 1 + \left( \frac{r_\perp}{r_{c_i}} \right)^2 \right]^{-3\beta_i + 1/2}, \quad (26)$$

where we found the following values as the best fit,

$$\begin{aligned} S_1 &= 1.4 \times 10^{-5} \text{ erg cm}^{-2} \text{ s}^{-1}, \quad r_{c1} = 210 \text{ kpc}, \quad \beta_1 = 0.44 \\ S_2 &= 6.0 \times 10^{-3} \text{ erg cm}^{-2} \text{ s}^{-1}, \quad r_{c2} = 2.8 \text{ kpc}, \quad \beta_2 = 0.45 \end{aligned} \quad (27)$$

deprojection

$$j(r) = \sum_{i=1}^2 \frac{S_i}{2\pi r_{ci}} \frac{6\beta_i - 1}{(1 + r^2/r_{ci}^2)^{3\beta_i}} \mathcal{B}\left(\frac{1}{2}, 3\beta_i\right), \quad (28)$$

where  $\mathcal{B}(a, b)$  denotes the beta-function (abrahamovich and stegun). (Pfrommer and ensslin 2003)

#### Normalization

The spatial and spectral part of the IR and UV have an arbitrary normalization where the specific energy density is given by  $u_{sd}^{cl}(E_{ph}, r) \propto u_{sd}^{gal}(E_{ph}) j(r)/j(0)$ . We fix the unitless normalization  $N$  using the total IR energy ( $E_{ir,vir}$ ) within  $r_{200}$

$$\begin{aligned} E_{ir,vir} &= L_{ir} \frac{r_{200}}{c} \\ &= N \int_{r_{200}} \int_{ir} \frac{j(r)}{j(0)} \frac{u_{ir}^{gal}(E_{ph})}{E_{ph}} dV dE_{ph}, \end{aligned} \quad (29)$$

where we in the first equality sign approximate the total energy of the IR photons within  $r_{200}$  with the IR luminosity  $L_{ir}$  [44] times the typical timescale it takes for a photon to propagate through the cluster (we assume that the cluster is optically thin). From [44] we

derive the following luminosity scaling relation,  $L_{ir} = 10^{21.7} \times (L_X/\text{erg s}^{-1})^{0.53} \text{erg s}^{-1}$ , where  $L_X$  is the X-ray luminosity within  $r_{200}$ .

#### Energy density

The energy density from starlight and dust in a galaxy cluster is given by

$$\begin{aligned} u_{sd}^{cl}(r) &= \int dE_{ph} \frac{d^2 N_{ph}^{cl}}{dE_{ph} dV} E_{ph} = \int dE_{ph} \frac{u_{sd}^{cl}(E_{ph}, r)}{E_{ph}} \\ &= N \frac{j(r)}{j(0)} \int dE_{ph} \frac{u_{sd}^{gal}(E_{ph})}{E_{ph}}. \end{aligned} \quad (30)$$

(DELETED TEXT)

### III. SPECTRAL GAMMA-RAY DISTRIBUTION

#### IV. SURFACE BRIGHTNESS PROFILES

#### V. POPULATION STUDIES

Model predictions

We wish to thank...

- 
- [1] M. Pato, L. Baudis, G. Bertone, R. R. de Austri, L. E. Strigari, *et al.*, (2010), \* Temporary entry \*, arXiv:1012.3458 [astro-ph.CO].
  - [2] J. R. Ellis, J. L. Feng, A. Ferstl, K. T. Matchev, and K. A. Olive, Eur.Phys.J. **C24**, 311 (2002), arXiv:astro-ph/0110225 [astro-ph].
  - [3] H. Baer, A. Mustafayev, S. Profumo, and X. Tata, Phys.Rev. **D75**, 035004 (2007), arXiv:hep-ph/0610154 [hep-ph].
  - [4] V. Khachatryan *et al.* (CMS Collaboration), (2011), \* Temporary entry \*, arXiv:1101.1628 [hep-ex].
  - [5] L. Bergstrom, New J.Phys. **11**, 105006 (2009), arXiv:0903.4849 [hep-ph].
  - [6] CTA, (2010), The CTA Consortium: Design Concepts for the Cherenkov Telescope Array, arXiv:1008.3703 [astro-ph.IM].
  - [7] L. Bergstrom, T. Bringmann, and J. Edsjo, (2010), \* Temporary entry \*, arXiv:1011.4514 [hep-ph].
  - [8] D. Hooper and L. Goodenough, ArXiv e-prints (2010), arXiv:1010.2752 [hep-ph].
  - [9] A. Boyarsky, D. Malyshev, and O. Ruchayskiy, ArXiv e-prints (2010), arXiv:1012.5839 [hep-ph].
  - [10] T. Bringmann, M. Doro, and M. Fornasa, JCAP **1**, 16 (2009), arXiv:0809.2269.
  - [11] V. A. Acciari, T. Arlen, T. Aune, M. Beilicke, W. Benbow, D. Boltuch, S. M. Bradbury, J. H. Buckley, V. Bugaev, K. Byrum, A. Cannon, A. Cesarini, J. L. Christiansen, L. Ciupik, W. Cui, R. Dickherber, C. Duke, J. P. Finley, G. Finnegan, A. Furniss, N. Galante, S. Godambe, J. Grube, R. Guenette, G. Gyuk, D. Hanna, J. Holder, C. M. Hui, T. B. Humensky, A. Imran, P. Kaaret, N. Karlsson, M. Kertzman, D. Kieda, A. Konopelko, H. Krawczynski, F. Krennrich, G. Maier, S. McArthur, A. McCann, M. McCutcheon, P. Moriarty, R. A. Ong, A. N. Otte, D. Pandel, J. S. Perkins, M. Pohl, J. Quinn, K. Ragan, L. C. Reyes, P. T. Reynolds, E. Roache, H. J. Rose, M. Schroedter, G. H. Sembroski, G. D. Senturk, A. W. Smith, D. Steele, S. P. Swordy, G. Tešić, M. Theiling, S. Thibadeau, A. Varlotta, V. V. Vassiliev, S. Vincent, R. G. Wagner, S. P. Wakely, J. E. Ward, T. C. Weekes, A. Weinstein, T. Weisgarber, D. A. Williams, S. Wissel, B. Zitzer, and VERITAS Collaboration, Astrophys. J. **720**, 1174 (2010), arXiv:1006.5955 [astro-ph.CO].
  - [12] P. Scott, J. Conrad, J. Edsjo, L. Bergström, C. Farnier, and Y. Akrami, JCAP **1**, 31 (2010), arXiv:0909.3300 [astro-ph.CO].
  - [13] M.-L. Garde, Talk at IDM10, Montpellier, France, July 2010, to appear in the Proceedings.
  - [14] A. Pinzke, C. Pfrommer, and L. Bergström, Physical Review Letters **103**, 181302 (2009), arXiv:0905.1948 [astro-ph.HE].
  - [15] L. Gao, C. S. Frenk, M. Boylan-Kolchin, A. Jenkins, V. Springel, and S. D. M. White, MNRAS **410**, 2309 (2011), arXiv:1006.2882 [astro-ph.CO].
  - [16] All halo masses and length scales in this paper are scaled to the currently favored value of Hubble's constant,  $H_0 = 70 \text{ km s}^{-1} \text{ Mpc}^{-1}$ . We define the virial mass  $M_{200}$  and virial radius  $r_{200}$  as the mass and radius of a sphere enclosing a mean density that is 200 times the critical density of the Universe  $\rho_{cr}$ .
  - [17] L. Gao, S. D. M. White, A. Jenkins, F. Stoehr, and V. Springel, MNRAS **355**, 819 (2004), arXiv:astro-ph/0404589.

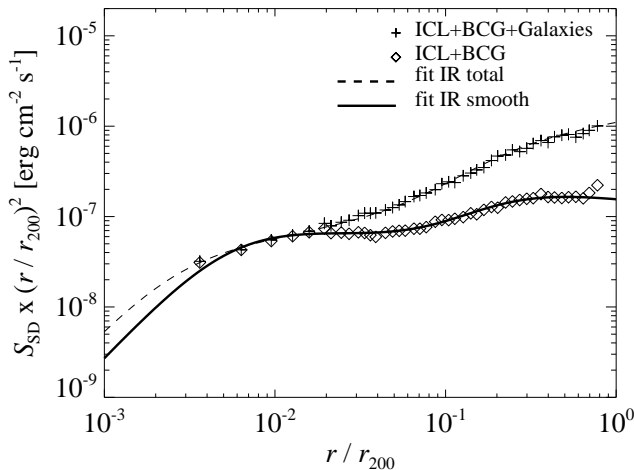


FIG. 3. Spatial dependence of light from dust and stars. We show 2D surface brightness profiles obtained from stacked clusters in the Sloan Digital Sky Survey (SDSS) at the redshift  $z \sim 0.25$  [43]. The brightness profiles have been weighted with the  $r_{200}$  normalized area inside radius  $r$ , and trace the radial dependence of the luminosity from stars and galaxies. The crosses show the total observed light including the diffuse intracluster (ICL), the galaxies, and the brightest cluster galaxy (BCG) in the center of the cluster. The diamonds denote the observed light from the ICL and the BCG. The solid line shows the fit to the data of the total light including the ICL, the BCG, and the galaxies, while the smooth component is represented by the dashed line that is fitted to only the ICL and the BCG.

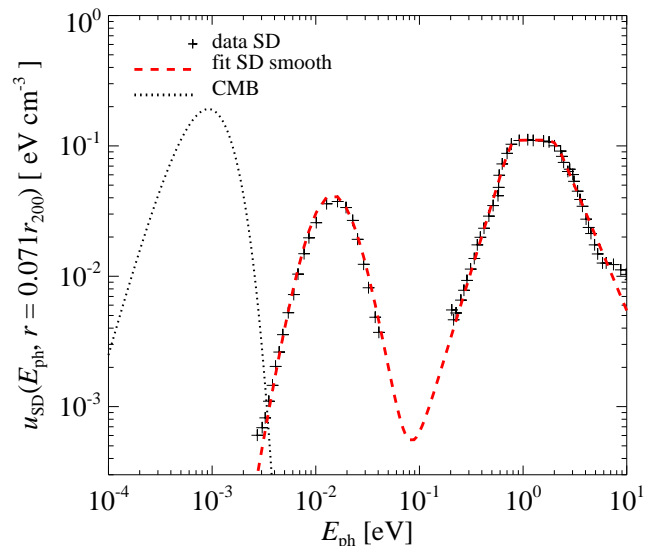


FIG. 4. Spectral dependence of radiation fields in a cluster of galaxies. The black dotted line in the left peak shows the spectrum of CMB photons using a black body with a temperature of 2.7 K. The crosses in the middle and right peaks represent the measured spectra from dust and stars (SD), respectively, and are derived in [41] for a galaxy. We normalize the individual spectra from SD separately using the observed luminosity from SD in clusters. The SD luminosity is related to the cluster mass through Eq. where we have used the mass  $M_{200} = 4.0 \cdot 10^{13} M_{\odot}$  in this figure. Finally we renormalize the SD spectra to the radius  $r = 0.071r_{200}$ , where the smooth energy density of the SD light (see fig 3) equals the energy density of the CMB. The red dashed lines show the fitted SD spectral model.

- [18] S. Colafrancesco, S. Profumo, and P. Ullio, *A&A* **455**, 21 (2006), arXiv:astro-ph/0507575.
- [19] T. E. Jeltema, J. Kehayias, and S. Profumo, *Phys. Rev. D* **80**, 023005 (2009), arXiv:0812.0597.
- [20] A. Pinzke and C. Pfrommer, *MNRAS* **409**, 449 (2010), arXiv:1001.5023 [astro-ph.CO].
- [21] J. F. Navarro, A. Ludlow, V. Springel, J. Wang, M. Vogelsberger, S. D. M. White, A. Jenkins, C. S. Frenk, and A. Helmi, *MNRAS* **402**, 21 (2010), arXiv:0810.1522.
- [22] A. V. Macciò, A. A. Dutton, and F. C. van den Bosch, *MNRAS* **391**, 1940 (2008), arXiv:0805.1926.
- [23] D. H. Zhao, Y. P. Jing, H. J. Mo, and G. Börner, *Astrophys. J.* **707**, 354 (2009), arXiv:0811.0828.
- [24] W. Hu and A. V. Kravtsov, *Astrophys. J.* **584**, 702 (2003), arXiv:astro-ph/0203169.
- [25] V. Springel, J. Wang, M. Vogelsberger, A. Ludlow, A. Jenkins, A. Helmi, J. F. Navarro, C. S. Frenk, and S. D. M. White, *MNRAS* **391**, 1685 (2008), arXiv:0809.0898.
- [26] M. Kuhlen, J. Diemand, P. Madau, and M. Zemp, *Journal of Physics Conference Series* **125**, 012008 (2008), arXiv:0810.3614.
- [27] V. Springel, S. D. M. White, C. S. Frenk, J. F. Navarro, A. Jenkins, M. Vogelsberger, J. Wang, A. Ludlow, and A. Helmi, *Nature (London)* **456**, 73 (2008), arXiv:0809.0894.
- [28] Our approach of fitting the scaling behavior of  $L_{\text{sub}}(< r)$  directly from numerical simulations self-consistently accounts for the radial dependence of the substructure concentration [25].
- [29] S. Hofmann, D. J. Schwarz, and H. Stöcker, *Phys. Rev. D* **64**, 083507 (2001), arXiv:astro-ph/0104173.
- [30] A. M. Green, S. Hofmann, and D. J. Schwarz, *JCAP* **8**, 3 (2005), arXiv:astro-ph/0503387.
- [31] J. C. Kempner, E. L. Blanton, T. E. Clarke, T. A. Enßlin, M. Johnston-Hollitt, and L. Rudnick, in *The Riddle of Cooling Flows in Galaxies and Clusters of galaxies*, edited by T. Reiprich, J. Kempner, & N. Soker (2004) pp. 335–+, arXiv:astro-ph/0310263.
- [32] L. Feretti, in *Astronomical Society of the Pacific Conference Series*, Astronomical Society of the Pacific Conference Series, Vol. 301, edited by S. Bowyer and C.-Y. Hwang (2003) pp. 143–+.
- [33] C. Ferrari, F. Govoni, S. Schindler, A. M. Bykov, and Y. Rephaeli, *Space Science Reviews* **134**, 93 (2008), arXiv:0801.0985.
- [34] V. S. Berezinsky, P. Blasi, and V. S. Ptuskin, *Astrophys. J.* **487**, 529 (1997).
- [35] M. Jubelgas, V. Springel, T. Enßlin, and C. Pfrommer, *A&A* **481**, 33 (2008), arXiv:astro-ph/0603485.
- [36] T. A. Enßlin, C. Pfrommer, V. Springel, and M. Jubelgas, *A&A* **473**, 41 (2007), arXiv:astro-ph/0603484.
- [37] C. Pfrommer, V. Springel, T. A. Enßlin, and M. Jubelgas, *MNRAS* **367**, 113 (2006), arXiv:astro-ph/0603483.
- [38] E. A. Helder, J. Vink, C. G. Bassa, A. Bamba, J. A. M. Bleeker, S. Funk, P. Ghavamian, K. J. van der Heyden,

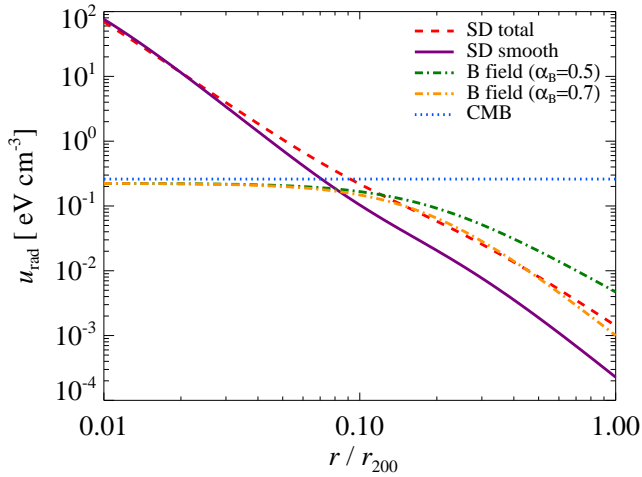


FIG. 5. Spatial dependence of the energy density of radiation fields in a cluster of galaxies. The energy density of the CMB, shown by the blue dotted line, is isotropic throughout the cluster, hence represented by a flat profile with  $u_{\text{cmb}} = 0.26 \text{ eV cm}^{-3}$ . The energy density of the light from dust and stars (SD) is denoted by the red dashed line and the solid purple line for the total SD light and the smooth SD light, respectively. The SD light has been renormalized to a cluster with the mass  $M_{200} = 4.0 \cdot 10^{13} M_{\odot}$ . Finally we show the energy density two magnetic field models with a central magnetic field of  $3 \mu\text{G}$ . The magnetic field scales with the gas density to the power  $\alpha_B$ ; green dash-dotted line ( $\alpha_B = 0.5$ ) and orange dash-dotted line ( $\alpha_B = 0.7$ ). Note that the SD radiation is dominating the energy density inside  $\sim 0.1 r_{200}$ .

- F. Verbunt, and R. Yamazaki, *Science* **325**, 719 (2009), arXiv:0906.4553 [astro-ph.GA].
- [39] H. Kang and T. W. Jones, *Astrophys. J.* **620**, 44 (2005).
- [40] T. Bringmann, L. Bergström, and J. Edsjö, *Journal of High Energy Physics* **1**, 49 (2008), arXiv:0710.3169 [hep-ph].
- [41] T. A. Porter, I. V. Moskalenko, and A. W. Strong, *ApJL* **648**, L29 (2006), arXiv:astro-ph/0607344.
- [42] R. C. Gilmore, P. Madau, J. R. Primack, R. S. Somerville, and F. Haardt, *MNRAS* **399**, 1694 (2009), arXiv:0905.1144 [astro-ph.CO].
- [43] S. Zibetti, S. D. M. White, D. P. Schneider, and J. Brinkmann, *MNRAS* **358**, 949 (2005), arXiv:astro-ph/0501194.
- [44] M. Giard, L. Montier, E. Pointecouteau, and E. Simmat, *A&A* **490**, 547 (2008), arXiv:0808.2404.
- [45] H. Mo, F. Bosch, and S. White, *Galaxy Formation and Evolution*, ISBN: 9780521857932 (2010).
- [46] W. C. Livingston, “Sun,” in *Allen’s Astrophysical Quantities*, edited by Cox, A. N. (2000) pp. 339–+.



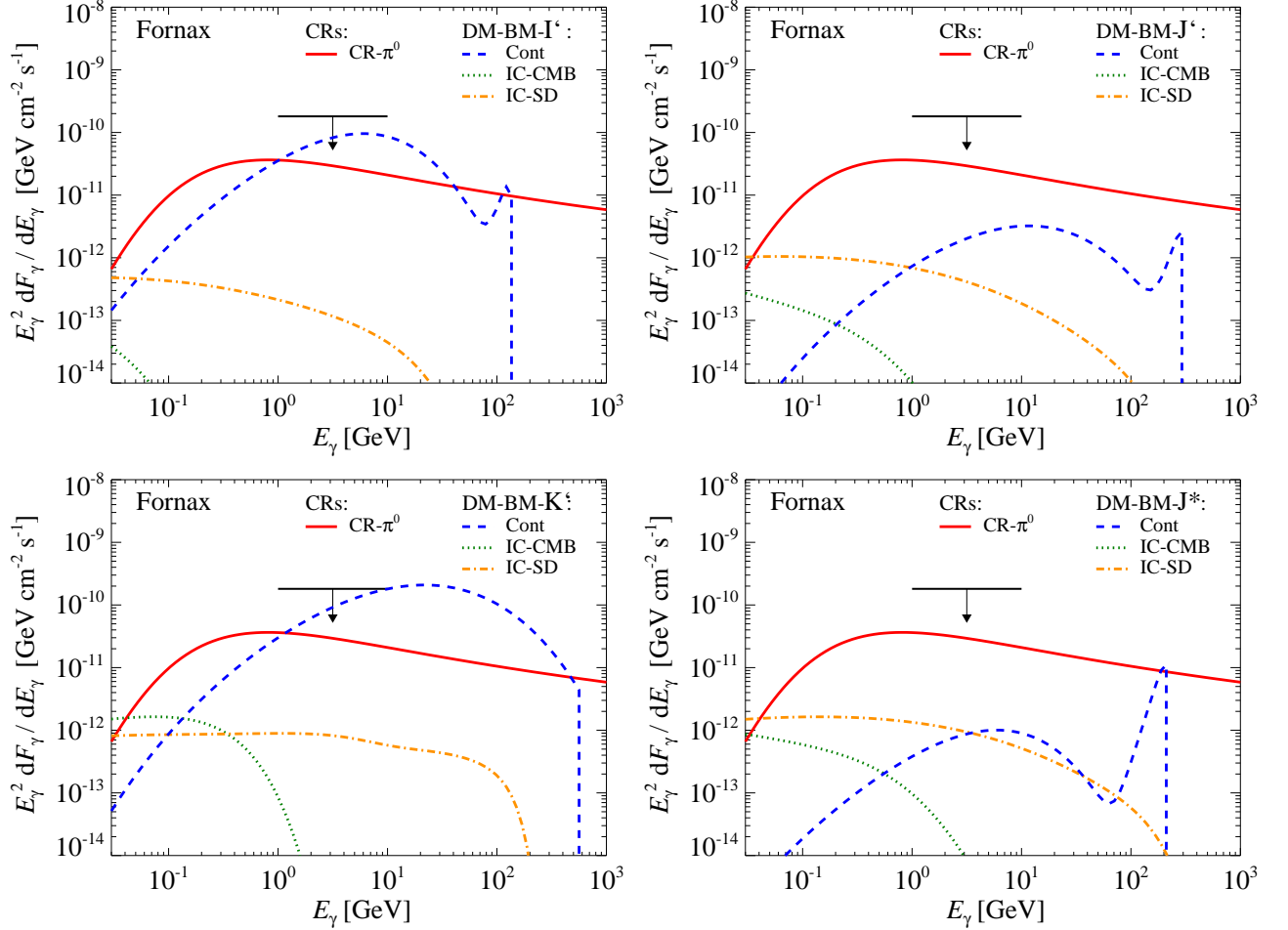


FIG. 6. Comparing the differential flux from different models: we show the continuum emission from DM benchmark (BM) models (blue), electrons and positrons from DM BM models that inverse Compton upscattered both CMB photons (orange) as well as dust and star photons (green), and CR induced gamma-ray emission (red solid). The various linestyles are associated with individual DM BM models; I<sup>\*</sup> (dotted), K<sup>\*</sup> (dashed), and J<sup>\*</sup> (dash-dotted). The emission is calculated for the Fornax cluster using a point spread function of 0.1 deg and a boost from substructures of ... We find bright prospects for detecting the continuum emission that is dominating the total emission in the GeV energy range. Also note that, above 100 MeV the total inverse Compton emission is at least a factor 10 smaller than the emission expected from both the continuum emission and the emission coming from CRs.

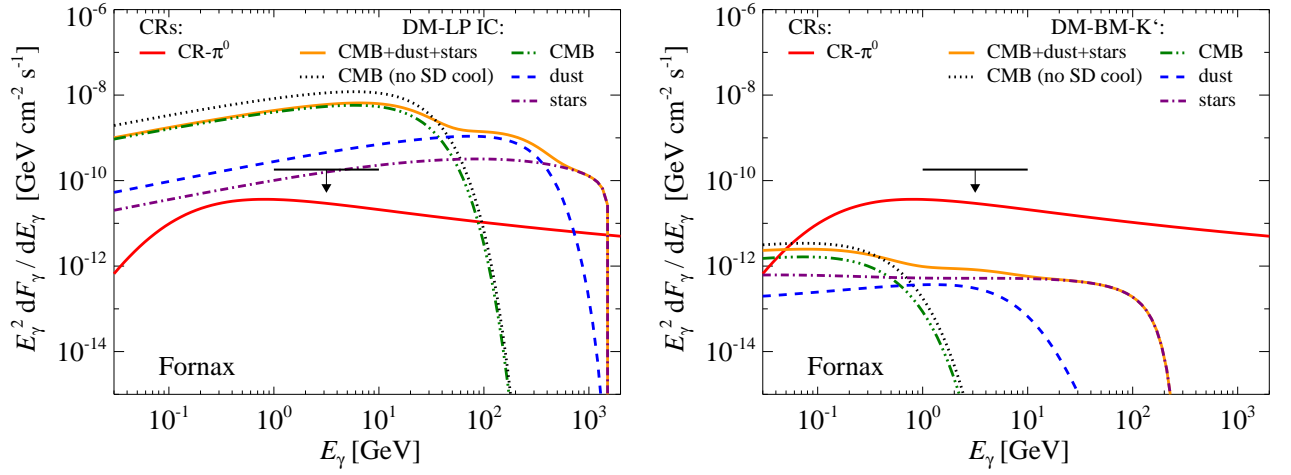


FIG. 7. Comparing the differential flux from different inverse Compton upscattered radiation fields in the Fornax cluster. We show the inverse Compton emissin induced by leptophilic DM in the left panel and by the K' benchmark model in the right panel. The contribution from each individual radiation field from top line to bottom line; CMB (green dashed-double-dotted), dust (blue dashed), stars (purple dashed-dotted). The sum of the three components are shown with the orange solid line. The black dotted line represents the upscattered CMB photons without any cooling from dust and stars. The red solid line show the CR induced gamma-ray flux. The black arrow show the differential upper limit from Fermi ADD REF. All fluxes are calculated within  $r_{200}$  with a point spread function of 0.1 deg. The boost from Sommerfeld is ..., and from substructures is .

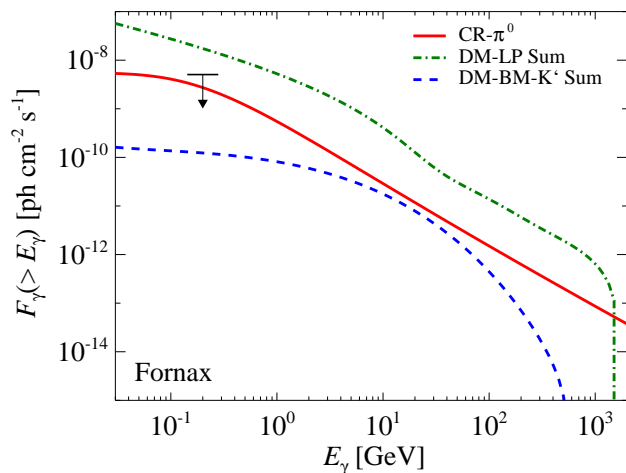


FIG. 8. Comparing the energy integrated flux from different models: we show the emission from leptophilic (LP) models with green lines, K' benchmark model (BM) with blue lines, and the CR induced emission with a red line. The dotted and dashed lines show the inverse Compton (IC) upscattered CMB photons and star and dust photons, respectively. The green solid line show the final state radiation from the LP model, and the solid blue line show the continuum emission from the DM. The black arrow show the integrated flux upper limit set by Fermi. The emission is calculated for the Fornax cluster using a point spread function of 0.1 deg and a boost from sub-structures of ... We find that LP models are dominating the total flux in the entire energy range, where the IC upscattered CMB photons overproduce the upper limit by a factor 3.

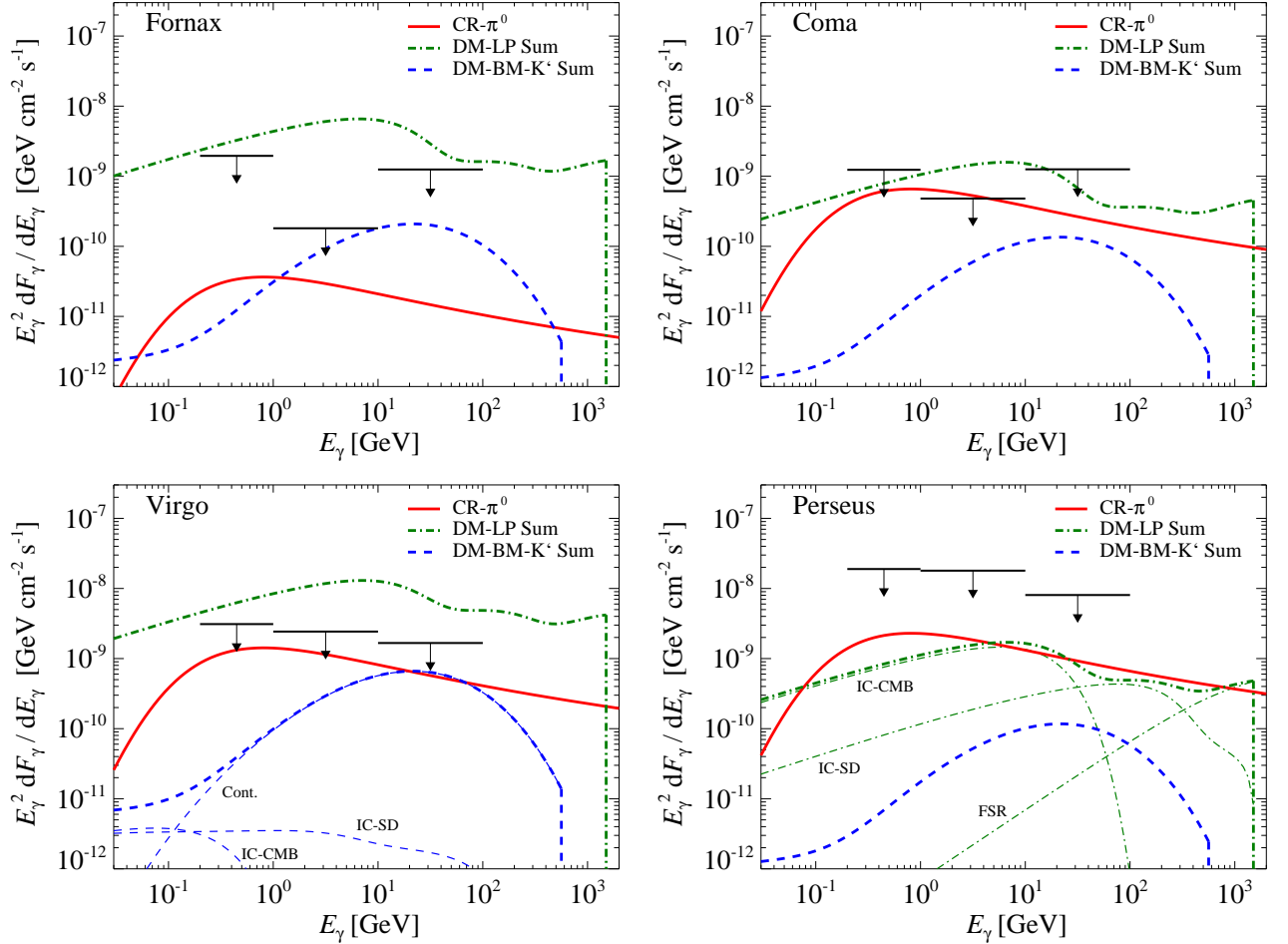


FIG. 9. Comparing the emission from different clusters. The emission from the clusters is calculated using a point spread function of 0.1 deg and includes the boost from substructures. We show the differential flux from four clusters; Fornax (upper left), Coma (upper right), Virgo (lower left), and Perseus (lower right). The different linestyles show; CR induced emission (solid), leptophilic models (LP) include both final state radiation and IC upscattered CMB, dust and star light (dotted), and benchmark K' models (BM) include continuum emission, and IC upscattered CMB, dust and star light (dashed). The arrows have colors matching each cluster and show the differential upper limits set by Fermi in the energy ranges 0.2 – 1 GeV, 1 – 10 GeV, and 10 – 100 GeV from left to right. For visualization we offset the arrows by increasing the mean energy by 30 percent in the opposite order as they appear in the figure, i.e. starting with Perseus. All fluxes are calculated within  $r_{200}$ . We find that the lower GeV energy regime is most constraining, and induce upper limits on boost factors.

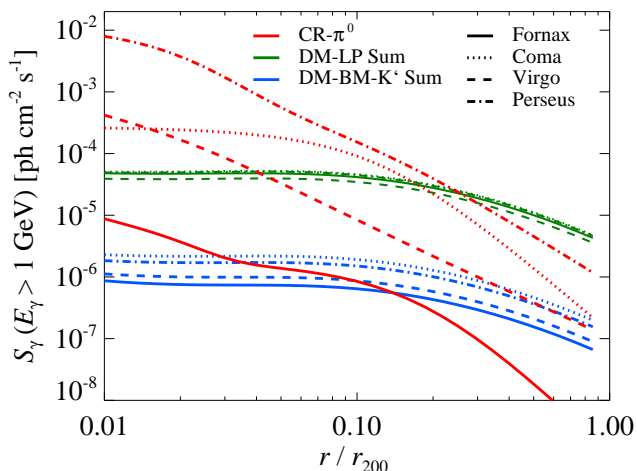


FIG. 10. Comparing the surface brightness from different clusters. We show the surface brightness above the energy 1 GeV. The boost from substructures is included and we use a point spread function of 0.1 deg.

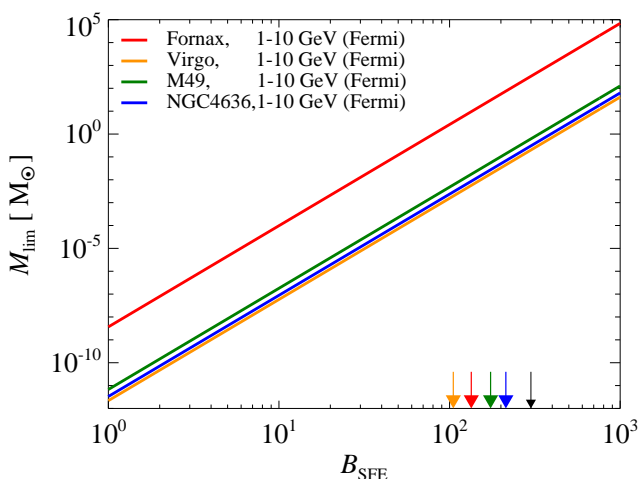


FIG. 11. Constraining leptophilic boost factors using flux upper limits. The emission is derived within  $r_{200}$  using a point spread function of 0.1 deg. In order not to overproduce the Fermi differential flux upper limits in the energy interval 1 – 10 GeV the boost from substructures and Sommerfeld enhancement (SFE) is constrained for four clusters; Fornax (red), Virgo (orange), M49 (green), and NGC4636 (Blue). The arrows have colors matching each cluster and indicate the SFE in each cluster. The SFE has been rescaled from 300 that is required to explain the electron and positron excess observed in the Milky Way (MW) with leptophilic dark matter (refer to equation). If the DM interpretation is correct, we can constrain the smallest size of halos to be larger than  $10 M_{\odot}$ . However, if the smallest size of DM halos is  $10^{-6} M_{\odot}$ , we can constrain the SFE to about 4 in Fornax, corresponding to a maximum SFE in the MW of about 10.

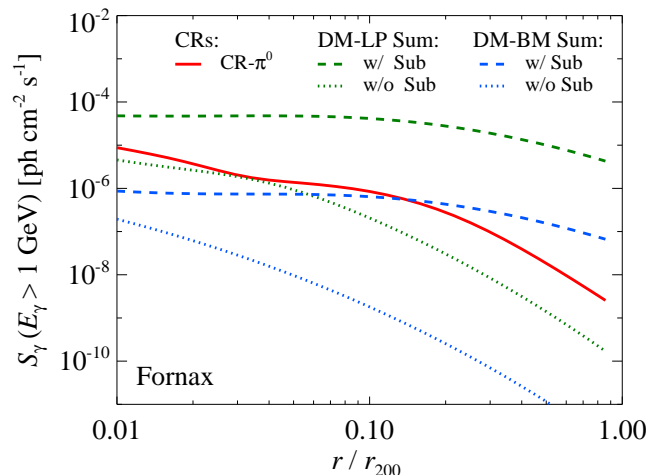


FIG. 12. The impact of substructures on surface brightness. We show the surface brightness at 1 GeV for the Fornax cluster using a very small point spread function of  $10^{-5}$  deg that reveals the details of the spatial profiles. The emission induced by CRs is denoted by the red solid line, the leptophilic models by green lines, and the DM  $K'$  benchmark model by blue lines. The dashed and dotted lines include and exclude substructures, respectively. Notice the nearly flat profiles when substructures are included, and the relative large boost at a percent of  $r_{200}$ .



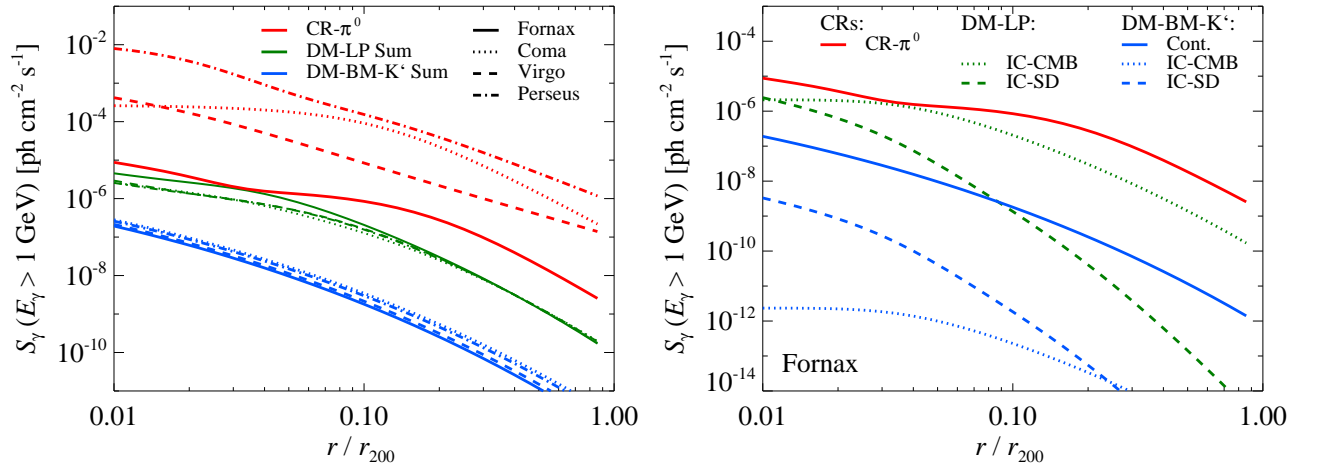


FIG. 13. The surface brightness without substructures. We show the CR induced emission (red), leptophilic emission (green), and emission from the  $K'$  benchmark model (blue). The surface brightness above 1 GeV is derived using a very small point spread function ( $\theta_{\text{psf}} = 10^{-5}$  deg). LEFT PANEL: compare the surface brightness for different clusters; Fornax (solid), Coma (dotted), Virgo (dashed), and Perseus (dash-dotted). RIGHT PANEL: compare different emission components in Fornax; dotted lines show the inverse Compton (IC) upscattered CMB photons, dashed lines show the IC upscattered photons from dust and stars, and blue solid line show the continuum emission from the  $K'$  benchmark model. **(DELETED TEXT)**

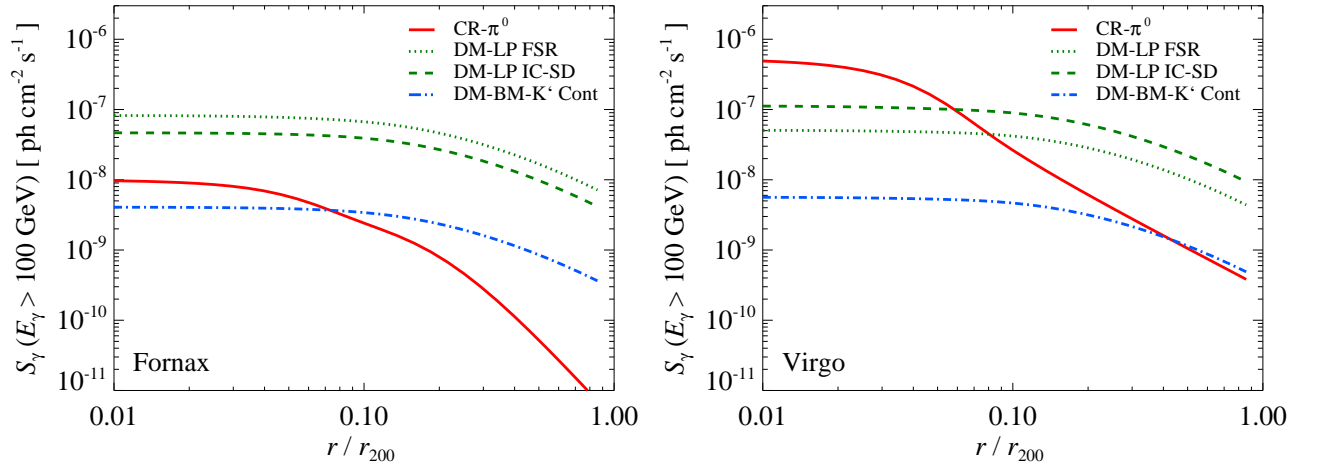


FIG. 14. Surface brightness predicted for Cherenkov telescopes. We show the emission above  $E_\gamma = 100$  GeV, include the boost from substructures and use a point spread function of 0.1 deg. Left panel show the Fornax cluster and right panel the Virgo cluster. The emission is derived for the following components; CRs (red solid), continuum emission from the DM  $K'$  benchmark model (blue dash-dotted), as well as final state radiation (green dashed) and inverse Compton upscattered dust and star light (green dotted) from leptophilic DM. **(DELETED TEXT)**

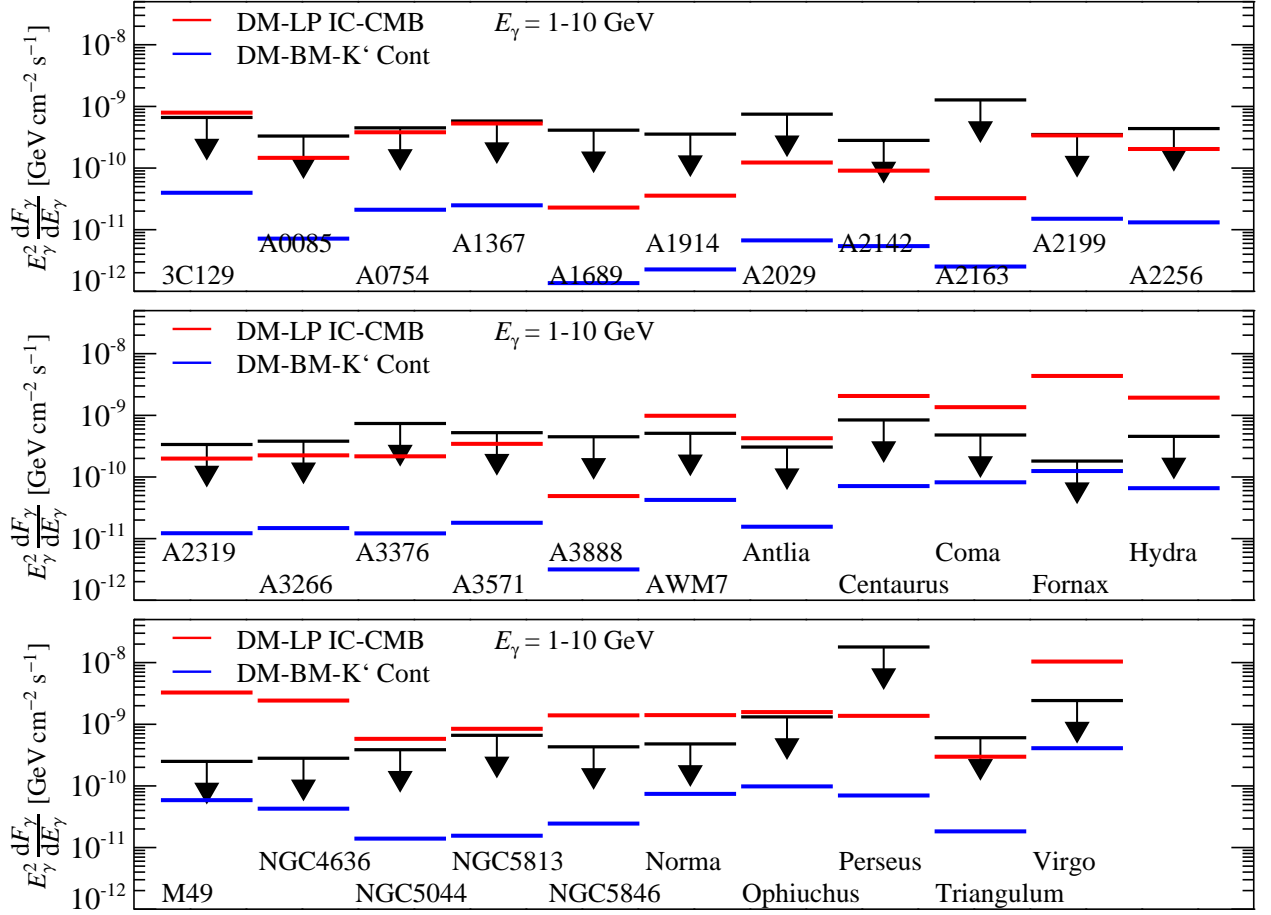


FIG. 15. *Fermi flux upper limits contrasted to the predicted DM gamma-ray flux.* We show the mean differential flux in the energy range  $E_\gamma = 1 - 10$  GeV for 32 clusters. The Fermi upper limits are shown with black arrows. The predicted fluxes are derived from both a leptophilic DM model that result in inverse Compton upscattered CMB photons (red), and the continuum emission from the DM K' benchmark model (blue). The leptophilic fluxes are ruled out by 14 of the clusters, with the strongest constraints set by Fornax and M49. We can not constrain the benchmark models, although our predictions are approaching the upper limits.

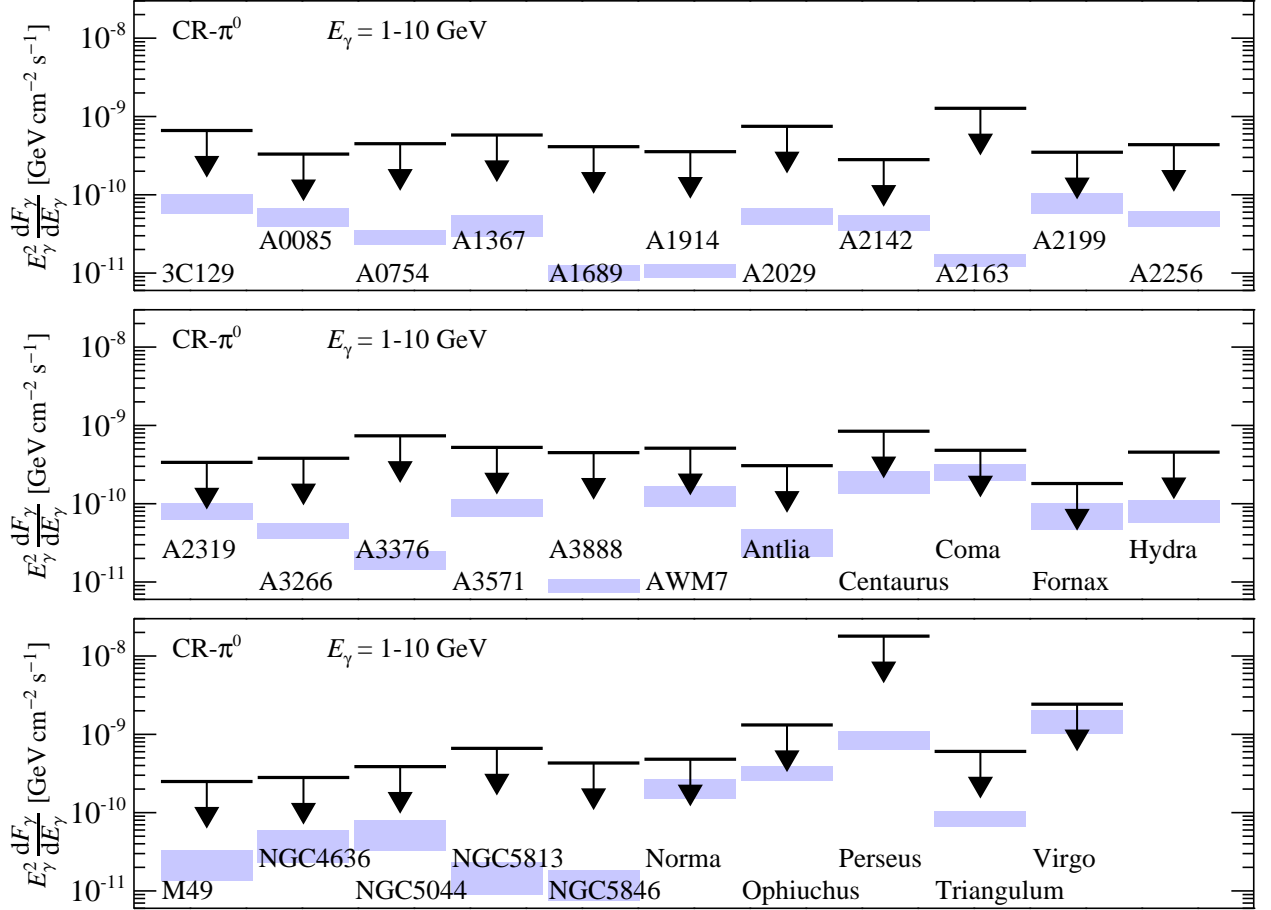


FIG. 16. Fermi flux upper limits contrasted to the predictions by the semi-analytic Pinzke and Pfrommer model for CR induced gamma-ray emission. We show the mean differential flux in the energy range  $E_\gamma = 1 - 10 \text{ GeV}$  for 32 clusters. The Fermi upper limits are shown with black arrows. The blue boxes show the gamma-ray emission from CR induced  $\pi^0$ s decaying, where the upper bound shows the estimates for an optimistic model and the lower bound a more conservative model excluding point sources (the realistic case is more likely in between, see [20] for details). Note that there is currently no tension between our predictions and upper limits from Fermi, although Virgo, Norma, and Coma are close and will in the coming years enforce constraints on the hadronic models.

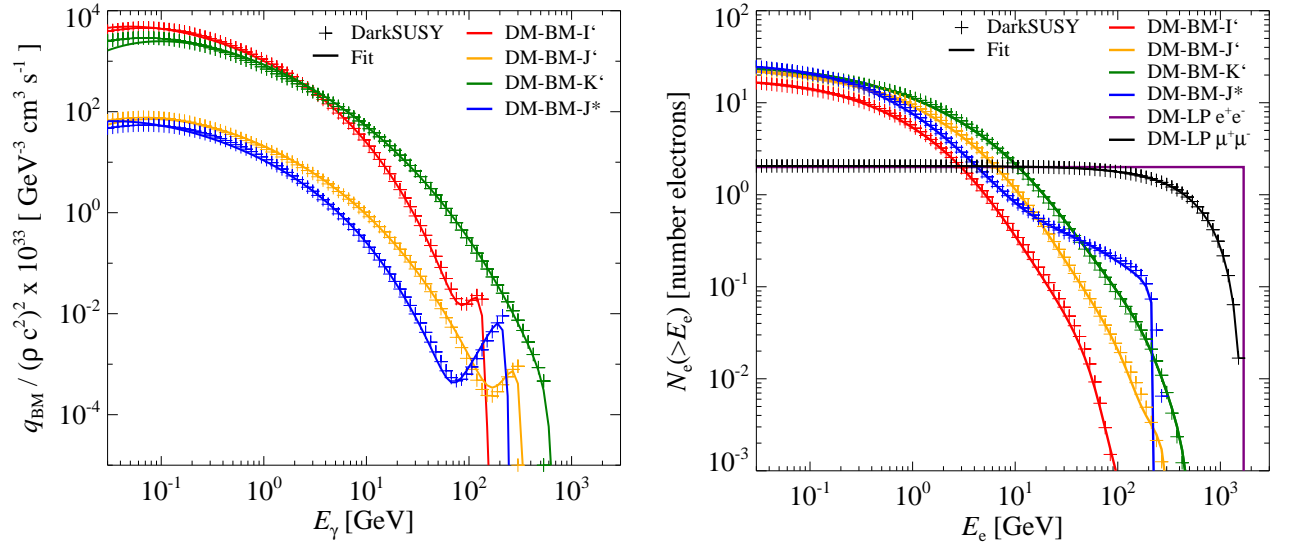


FIG. 17. The underlying source functions for different DM models. Crosses show the simulated data from *DarkSUSY* and the solid lines show the fit to the data using Eq.... LEFT PANEL: normalized differential continuum spectra for four different DM benchmark (BM) models;  $I'$  model (red),  $J'$  (orange),  $K'$  (green), and  $J^*$  (blue). RIGHT PANEL: number of electron and positron per DM annihilation above the electron energy  $E_e$  for different dark matter models;  $I'$  BM model (red),  $J'$  BM model (orange),  $K'$  BM model (green), and  $J^*$  BM model (blue), leptophilic (LP) DM annihilating into electrons and positrons (purple), and LP DM annihilating into muons (black).

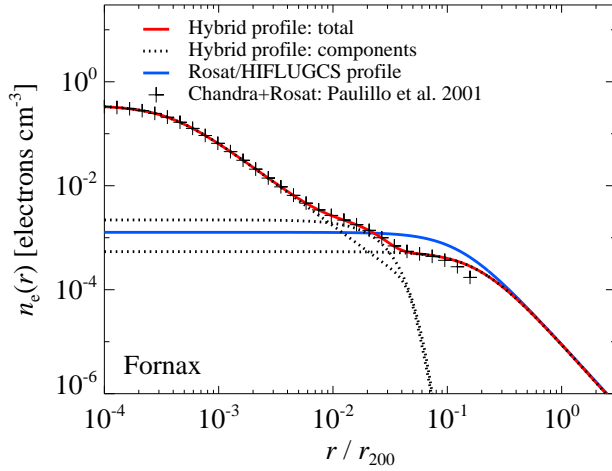


FIG. 18. Comparing different electron number density profiles for the Fornax cluster. Black crosses show the density profile inferred from deprojected Chandra and Rosat X-ray surface brightness observations CITE. The total hybrid profile shown by the red solid line represent the best fit to the data, where the fitted individual density components are shown by the black dotted lines. The blue solid line show the single beta density profile inferred from the HIFLUGCS catalogue. Due to insufficient sensitivity to the outer part in the plotted data, we infer the outer slope found in the HIFLUGCS catalogue.

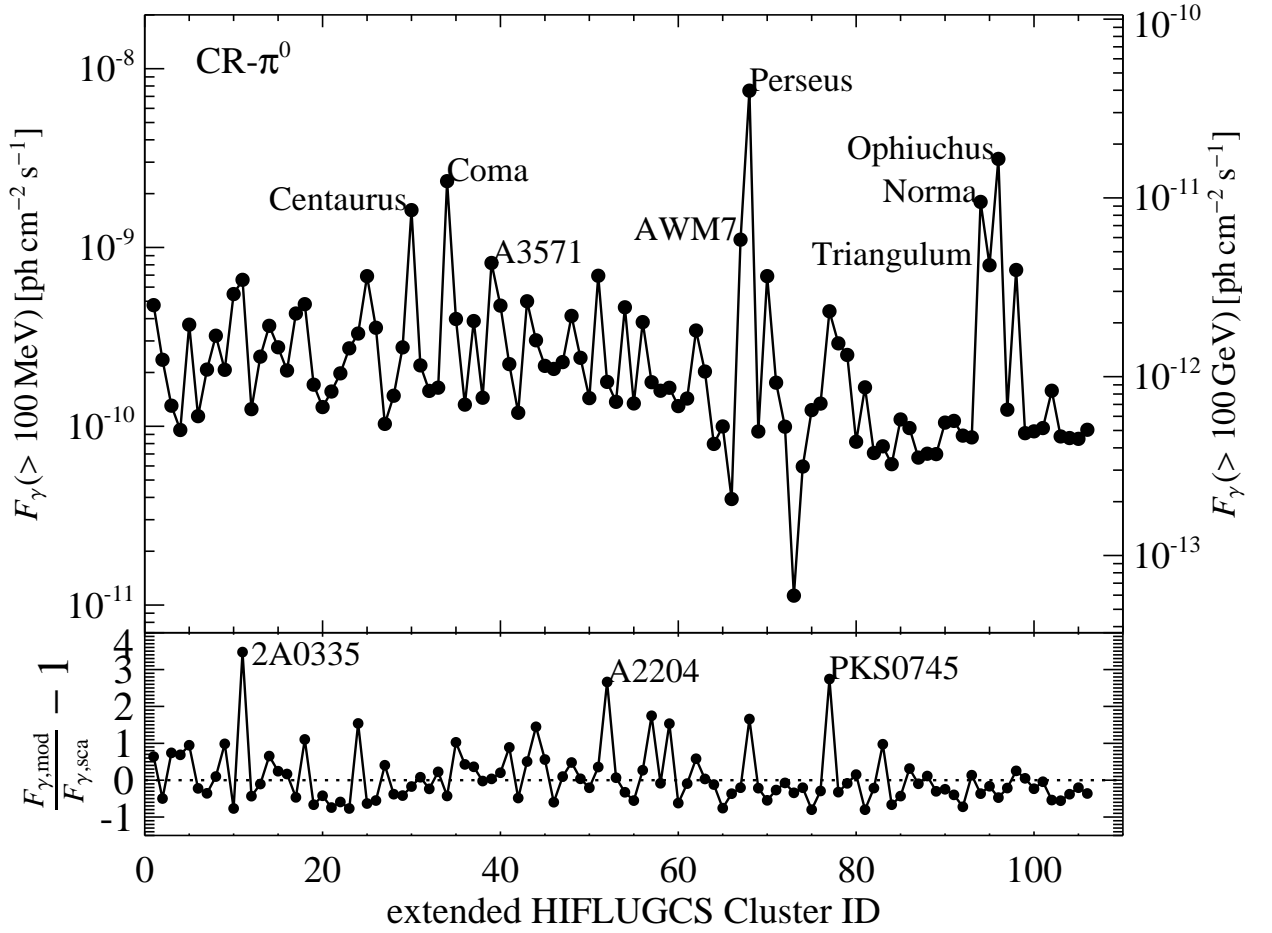


FIG. 19. Comparing the flux from clusters in the extended HIFLUGCS catalogue. We show the energy integrated gamma-ray flux induced by CRs for the 106 clusters included in the extended HIFLUGCS catalogue. The fluxes are calculated within  $r_{200}$ , and are derived using a single beta profile for each cluster's gas density profile (see text for details). The upper panel show the energy integrated flux above 100 MeV (left side) and above 100 GeV (right side), both as a function of HIFLUGCS cluster ID. The name of the eight brightest clusters are written out. The lower panel show the relative difference between the gamma-ray flux predicted by mass-luminosity scaling relations compared to the flux computed using the semi-analytically model CITE. The name of the clusters with the largest offset are printed out, which correlate with cool core clusters.



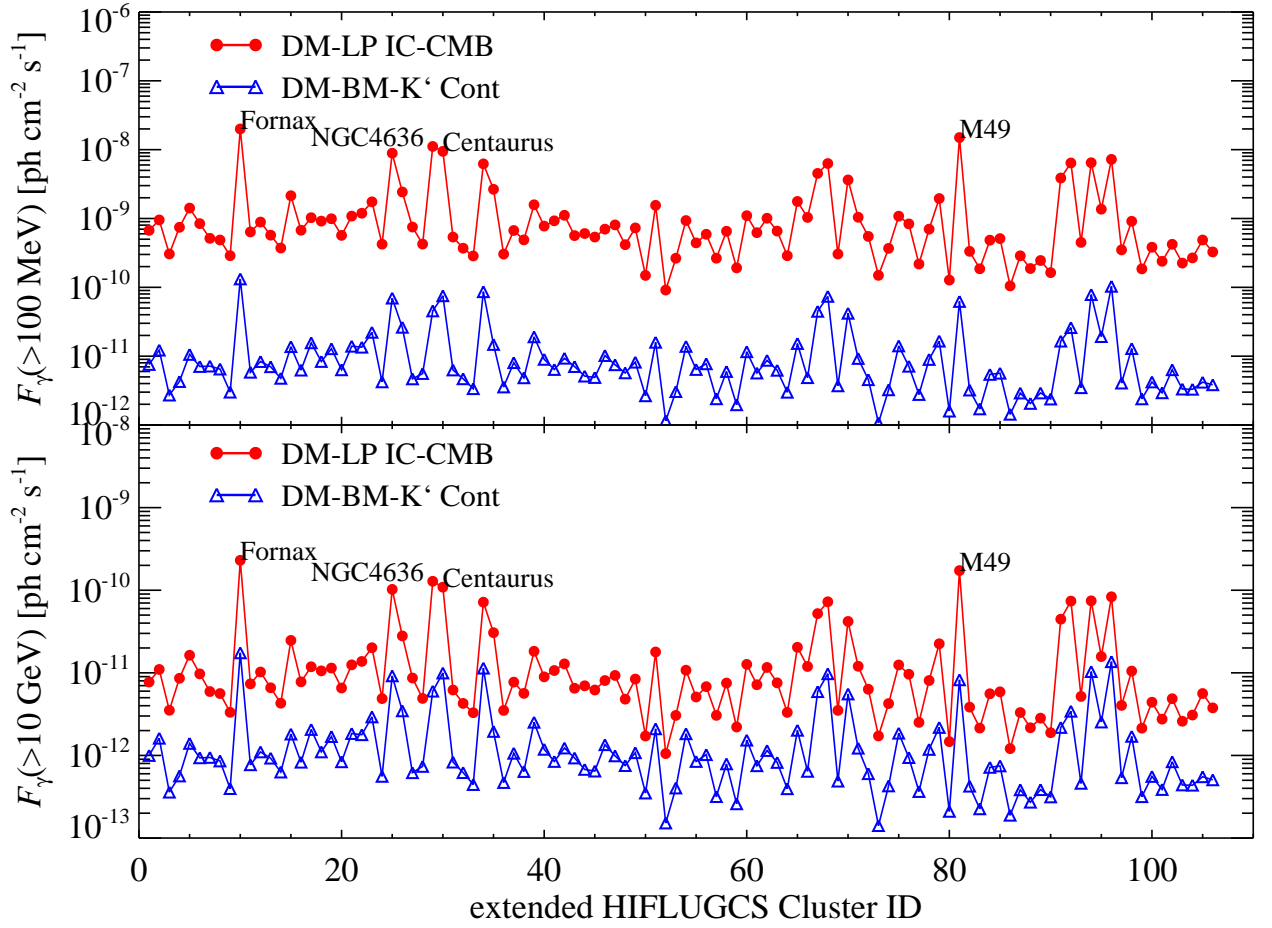


FIG. 20. Comparing the flux from clusters in the extended HIFLUGCS catalogue. We show the energy integrated gamma-ray fluxes derived from both leptophilic DM that result in inverse Compton upscattered CMB photons (red), and the continuum emission from the DM  $K'$  benchmark model (blue). The fluxes are calculated within  $r_{200}$  for each of the 106 clusters included in the extended HIFLUGCS catalogue, and are derived using a single beta profile for each cluster's gas density profile (see text for details). The upper panel show the energy integrated flux above 100 MeV and the lower panel above 10 GeV, both as a function of HIFLUGCS cluster ID. The name of the four brightest clusters are written out, where Fornax and M49 are the brightest targets.